Elastocaloric effects in polycrystalline Ni-Fe-Ga foams with hierarchical pore architecture

Muhammad Imran [1,2] and Xuexi Zhang [1,*]

[1] *School of Materials Science and Engineering, Harbin Institute of Technology, Harbin 150001, China*
[2] *Mechanical Engineering Department, University of Engineering & Technology Taxila, Taxila 47050, Pakistan*

Ni-Fe-Ga foam with hierarchical pore architecture was created by replication casting. The annealed foam had an open porosity 53% and reversible superelasticity with recoverable strain 4.9%. An adiabatic temperature change of 4.1 K with low hysteresis and coefficient of performance 22 were obtained under an external stress 70 MPa. The foam showed improved cyclic stability ($\sim$2.8 K in 194 cycles) because of low hysteresis loss under small stress and high crack initiation/propagation resistance in small size nodes and struts, which demonstrated a feasible strategy to enhance the mechanical and functional stabilities of ferromagnetic shape memory alloys via tailoring the material architectures. Nevertheless, the achieved elastocaloric cooling stability still cannot satisfy (10^7 cycles) the commercial application, therefore, it should be further explored to become a promising candidate for elastocaloric material.

In recent decades, solid-state refrigeration based on elastocaloric effects (eCE) has been emphasized over vapor compression technology because of high compactness, efficiency, and ecofriendliness [1]. When the applied uniaxial stress varies its intensity adiabatically/isothermally, a temperature change or entropy variation may occur in eCE materials [2,3]. Large adiabatic temperature changes (ΔT_{ad}) have been demonstrated in some conventional (NiTi [4,5] and Cu-based [6]) and ferromagnetic (Ni-Mn-[7,8] and Ni-Fe based [9]) shape memory alloys (SMAs). Although NiTi alloys are employed in many eCE prototypes due to large ΔT_{ad} and good mechanical properties [10], albeit ferromagnetic (FM)SMAs undergo stress-induced martensite transformation (SIMT) at much lower stress which is useful for miniaturized eCE refrigeration [11,12].

Among these, Ni-Fe-Ga (FMSMAs) exhibited attractive eCE properties because of their low cost and high ductility with favorable mechanical properties [13,14]. Excellent ΔT_{ad} (7.5–13.5 K) with high cyclic stability (over 10^4 cycles) has been confirmed in Ni-Fe-Ga single crystals [12,15,16]. However, the fabrication of single crystals is difficult and time consuming [17]. By contrast, polycrystalline Ni-Fe-Ga alloys may be produced via low-cost casting, but they are brittle and have a high intergranular fracture tendency during martensite transformation [18]. As a result, polycrystals of Ni-Fe-Ga alloys rarely show stable eCE during (10–100) cycles [18], which seriously restricts their application for commercial cooling [19,20].

Therefore, numerous approaches have been employed to improve the working stability of SMAs, e.g., adjusting the stress mode [20], surface finishing [21], introducing texture [22], toughening via secondary phase [18], microalloying

[23], and grain refinement [24]. Given that the mechanical instability of polycrystals is induced by grain boundary constraints, it is possible to decline the constraints via introducing pores in polycrystals. For instance, Ni-Mn-Ga polycrystals with 76% porosity showed stable magnetic field induced strain (MFIS) over 25 million magneto-mechanical times [25]. La(Fe, Si)$_{13}$ porous alloys with $\sim$25% porosity demonstrated superior cyclic stability ($<10^3$ cycles) and low thermal hysteresis over counter bulk part (only four cycles) for magnetocaloric effect [26]. Similarly, our previous studies revealed that Ni-Fe-Ga single pore foam effectively employed as an elastocaloric refrigerant [27] with better eCE cyclic stability (10^2 cycles) than the bulk alloy (32 cycles) through reducing the hysteresis energy loss [28]. Additionally, porous alloys with open pores have a high specific surface area and thus heat exchange efficiency with surrounding agents [29,30].

Herein, we report an approach of tailoring the material's architecture to further increase the cyclic stability by creating hierarchical pores in Ni-Fe-Ga polycrystals through a replication casting method. The dual pore foam has a porosity 53% and a fully reversible superelastic response (4.9%) at room temperature. A stable ΔT_{ad} 4.1 K with large specific cooling strength ($|\Delta T/\Delta\sigma|$) 58.6 K/GPa and coefficient of performance for materials (COP) 22 under an external stress 70 MPa and eCE cyclic stability up to 194 times were demonstrated with high crack initiation and propagation resistance in nodes and struts with size smaller than grains.

Vacuum induction melting was employed to prepare $Ni_{52.8\pm0.30}Fe_{18.7\pm0.06}Ga_{28.5\pm0.70}$ (at. %) parent billets from high purity elements Ni, Fe and Ga ($>99.99\%$). The preparation process of dual pore foams via replication casting technique was similar to that of the Ni-Mn-Ga alloy [31] and is briefly described here (Supplemental Material Fig. S1a) [32]. Large NaAlO$_2$ space holder particles (diameter 350–500 µm)

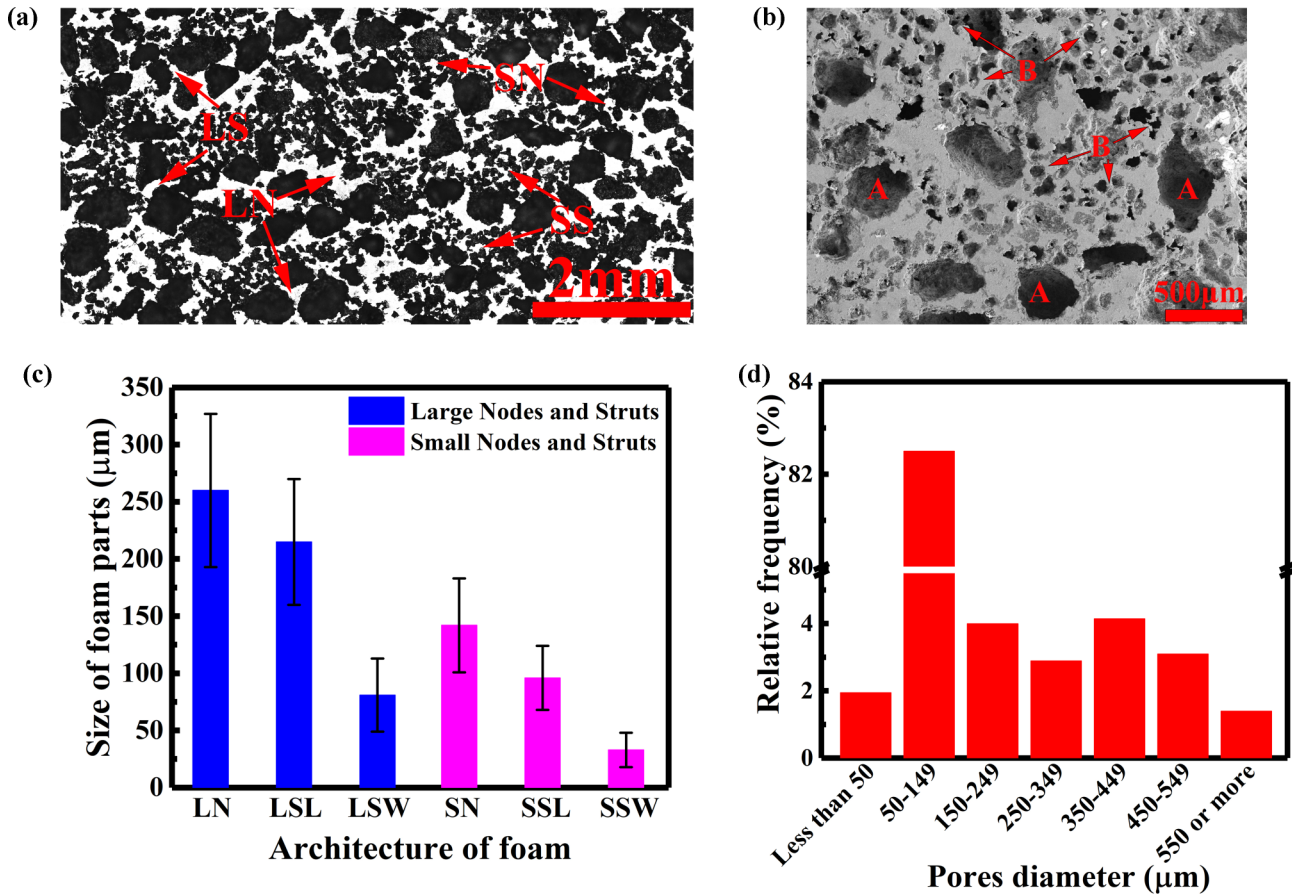*Corresponding author: xxzhang@hit.edu.cn

FIG. 1. The structural characterization of Ni-Fe-Ga foam with hierarchical pore architectures. (a) Optical micrograph showing the architecture of foam (i.e., LN: large nodes; LS: large struts; SN: small nodes; and SS: small struts), while (b) both large (A) and small (B) pores are depicted in SEM picture. Image analysis provides the (c) mean size of various large/small nodes and the dimensions of the struts (i.e., LSL: large strut length; LSW: large strut width; SSL: small strut length; and SSW: small strut width) along with (d) the distribution of pore sizes in Ni-Fe-Ga foam with 53% porosity.

were first poured into the alumina crucible filled with acetone (1). By controlling the powder mass, the particles just formed a close packed single layer after settling down (2). Then small $NaAlO_2$ particles (diameter 70–90 µm) were poured into the crucible, which was allowed to settle between the gap of large particles (3,4). The above process was repeated several times until a designed height was reached (5). The crucible was heated at 321 K for 24 h to remove acetone and then sintered at 1773 K for 3 h to create the $NaAlO_2$ preform (6). Finally, the preform was evacuated to ∼3.8×10^{-3} Pa, heated to a temperature 1603 K at a rate of 7 K/min to melt the alloy and infiltrated with melting Ni-Fe-Ga alloy under a pressure 1.34 atm. After infiltrating, the alloy was cooled to room temperature inside the furnace.

The prepared Ni-Fe-Ga/$NaAlO_2$ composite was immersed in mixed acids 2% HF + 10% H_2SO_4 and treated under sonication for 2400 min, as shown in Fig. S1b [32]. The mass loss rate is high at the beginning but gradually decreased after 1600 min, because of the reduced content of $NaAlO_2$ exposed to acids. A porosity of 48.5% was reached at the end of stage I (2400 min). After the sample was moved into a 2% HF + 10% HNO_3 acid bath and sonicated for 10 min, followed by treatment in 2% HF + 10% H_2SO_4 acids, the mass loss rate increased again because the 2% HF + 10% HNO_3 solution

may dissolve the Ni-Fe-Ga alloy while 2% HF + 10% H_2SO_4 cannot.

In stage II, $NaAlO_2$ particles encapsulated by alloys were exposed to acids and thus removed, which resulted in the complete removal of $NaAlO_2$ and a final porosity 53%. By this means, high integral nodes and struts showing a hierarchical architecture, which are crucial for carrying loads by plastic hinging or bending under compression [33], were obtained (Fig. 1). Homogeneous distribution of the large (A) and small (B) pores along with the structural architecture of foam, i.e., the large /small nodes and struts, can be observed in Figs. 1(a) and 1(b). An image analysis was carried out to characterize the architecture of hierarchical pore foam through pore size distribution and wall thickness, as illustrated in Figs. 1(c) and 1(d). The large/small nodes varied from 193 to 327 µm and 101 to 183 µm in length, respectively. Similarly, the length of large struts changed from 160 to 270 µm with the average width of 81 µm, while the length of small struts fluctuated from 70–123 µm with the average width of 33 µm [see Fig. 1(c)]. From the image analysis of Ni-Fe-Ga foam [Fig. 1(a)], 924 pores were obtained with various diameters (38–650 µm), which were divided into $n = 7$ intervals for pore size characterization. As a result, the pore size distribution curve was plotted between the relative frequency and pore

diameters [Fig. 1(d)]. The diameters range between 50 and 550 μm exhibited the maximum pores of ~97%, which are strongly correlated to the originally designed values. Moreover, the highest frequency of 82.5% confirmed the existence of small pores (50–150 μm diameters) compared to the 7.25% large pores (350–550 μm diameters).

The foam specimens with size $4 \times 4 \times 8$ mm^3 were cut through a diamond saw and annealed at a temperature 1453 K for 5 h, then quenched in water to create a single β-phase state. The composition of the annealed foam was determined to be $Ni_{52.9\pm0.59}Fe_{19.2\pm0.21}Ga_{27.9\pm0.56}$ (at. %) by energy dispersive spectroscopy on a scanning electron microscope (SEM, Zeiss Supra 55 SAPPHIRE). The microstructure was characterized by an Olympus PMG3 optical microscope and PANalytical Empyrean x-ray diffraction (XRD) with Cu-Kα radiation under the reflection mode. TA Q-200 differential scanning calorimeter (DSC) with the heating/cooling rates of 10 K/min was utilized to study the martensite transformation (MT) behavior. Instron 5569 and 5982 universal testing machines were employed to conduct compression experiments at room and elevated temperatures, respectively. The compressive superelastic tests were performed with strain rate-driven mode (lower 1.7×10^{-4} s^{-1} and higher 2.0×10^{-2} s^{-1} strain rates were used for isothermal and adiabatic conditions, respectively) under constant external stresses (50–70 MPa). The ΔT_{ad} and local temperature evolution were detected by infrared (IR) thermography (FLIR A325sc) with frame rate 30 Hz, 320×240 pixels, spatial resolution 25 μm and measurement accuracy $\pm2\%$. The black paint (emissivity = 0.95) was used on foam sample to decrease the reflection of natural light with increasing the emissivity of sample surface.

The XRD spectrum confirmed the cubic L2$_1$ austenite (β-phase) in dual pore foam, which has lattice parameter (a) 5.75 Å at room temperature, as shown in Fig. S2 [32]. The MT temperatures for dual pore foam, i.e., $M_f = 280$ K, $M_s = 286$ K, $A_s = 288$ K, and $A_f = 293$ K, were evaluated by the intersection of base and tangent lines, as shown in Fig. S3 [32]. The MT entropy change can be computed by $\Delta S = \Delta H / T_0 (10.7$ J/kg K), where ΔH is the enthalpy change (3.1 J/g) and T_0 is the equilibrium temperature $T_0 = (M_s + M_f)/2 = 289.5$ K. The low thermal hysteresis $(A_f - M_s = 7K)$ facilitated the reversible superelasticity. The theoretical adiabatic temperature change (ΔT_{th}) can be estimated by $\Delta T_{th} = L/C_p = 9.54$ K, where C_p is the specific heat capacity (325 J/kg K) [28].

Figure 2(a) shows the compressive superelastic plots of the annealed Ni-Fe-Ga foam at a temperature 296 K, slightly higher than $A_f = 293$ K. The foam showed a large recovery strain (ε_{rec}) 4.9% under external stress 60 MPa. The obtained ε_{rec} is superior to NiTi [34] (2% ε_{rec} under 45% porosity) and Cu-Al-Ni [35] (2.6% ε_{rec} under 58% porosity) foams.

Moreover, based on the superelastic curves at various temperatures (296–311 K, Fig. S4a [32]), the temperature-dependent critical stresses during forward $(\frac{d\sigma_{Ms}}{dT} = 0.9$ MPa/K) and reverse $(\frac{d\sigma_{As}}{dT} = 1.3$ MPa/K) MTs are determined (Fig. S4b [32]), which are comparable to some other SMAs, e.g., Co-Ni-Ga (2.0 MPa/K) [36], Fe-Pd (1.0 MPa/K) [37], and Ni-Fe-Ga (1.4 MPa/K) [16]. According to the Clausius–Clapeyron relation $\Delta S_{c-c} = -\frac{1}{\rho} \frac{d\sigma}{dT} \varepsilon_{tr}$, the values of stress-induced entropy

changes ($\Delta S_{c-c} = 2.30$ J/kg K, 2.62 J/kg K and 3.0 J/kg K under 50, 60, and 70 MPa, respectively) during forward MT can be determined at 296 K, where $\frac{d\sigma_{Ms}}{dT}$ (0.9 MPa/K) is the temperature dependent critical stress (austenite →martensite phase), ρ (8235 kg/m^3) is mass density and ε_{tr} is MT strain (2.1%, 2.4% and 2.8% accordingly). In order to achieve the maximum ΔS estimated from DSC, the much larger stress value is required to achieve the complete MT, which seems higher than the fracture limits in our foam samples [see Fig. 2(a)]. In addition, the transformation strains and corresponding entropy changes measured from the Clausius-Clapeyron relation during forward MT in Ni-Fe-Ga foam under various stresses (50, 60, and 70 MPa) and different temperatures (296, 301, 306 and 311 K) are summarized in Fig. S5 [32]. Furthermore, the less adiabatic temperature change ($\Delta T_{c-c} = T \Delta S / C_p = 2.09$, 2.4, and 2.73 K under 50, 60, and 70 MPa, respectively) estimated from the Clausius-Clapeyron expression may also be attributed to the incomplete MT under low isothermal applied stresses.

Figure 2(b) displays directly measured adiabatic temperature change (ΔT_{ad}) during loading and unloading processes at a strain rate of 0.02 s^{-1}. ΔT_{ad} increases with increasing applied stresses due to a large fraction of SIMT. Under an external stress 60 MPa, ΔT_{ad} is determined to be 3.4 K during loading and -3.3 K during unloading, which is in good agreement of $\Delta T_{c-c} = 3.5$ K. The maximum ΔT_{ad} 4.1 and 3.8 K is obtained during loading and unloading, respectively, under higher stress 70 MPa, which is still less than $\Delta T_{th} = 9.5$ K evaluated via DSC.

The smaller ΔT_{ad} may ascribe the nonideal adiabatic condition [38] with inhomogeneous temperature distribution [28] due to various sizes of struts, nodes, and pores, which was determined from the whole sample surface through "Mean" temperature mode (averaging the nodes and struts temperature). Furthermore, the struts and nodes were not only deformed due to bending or hinging but also axially deformed under compression [33]. Therefore, the inhomogeneous SIMT occur in various (i.e., the bending/hinging and axially deformed) parts, which causes the less eCE activity under bending or plastically hinging parts due to higher stress concentration at the connection sites between nodes and struts. Finally, in comparison to estimated value, the annealed foam exhibited lower ΔT_{ad} under bending parts of material. Nevertheless, the measured ΔT_{ad} 4.1 K in the present Ni-Fe-Ga foam is comparable to some well-studied eCE alloys including $Ni_{54}Fe_{19}Ga_{27}$ (4.0 K) [18], $Ni_{45}Mn_{44}Sn_{11}$ (4.0 K) [11], $Ni_{45.7}Mn_{36.6}In_{13.3}Co_{5.1}$ (3.5 K) [39], $Cu_{68}Al_{16}Zn_{16}$ (4.0 K) [40], and $Ni_{32.5}Ti_{54.9}Cu_{12.6}$ (4.1 K) [41].

To reveal the temperature profile throughout the sample surface, a series of infrared images were taken at an interval ~0.72 s [see Fig. 2(c)] during a cycle under 70 MPa. It is worth noting that ΔT_{ad} is not uniform on foam specimen due to various geometries of struts and nodes, as shown in the inset of Fig. 2(a). In addition, the local stress concentration at sharp tips of pores is favorable for SIMT even at low nominal stress [42], while the thinner struts and nodes may homogeneously drive a higher percent of SIMT [43] in the present hierarchical foam.

Application of an eCE material also requires high working stability. We carried out multiple compressive cycles at 296 K
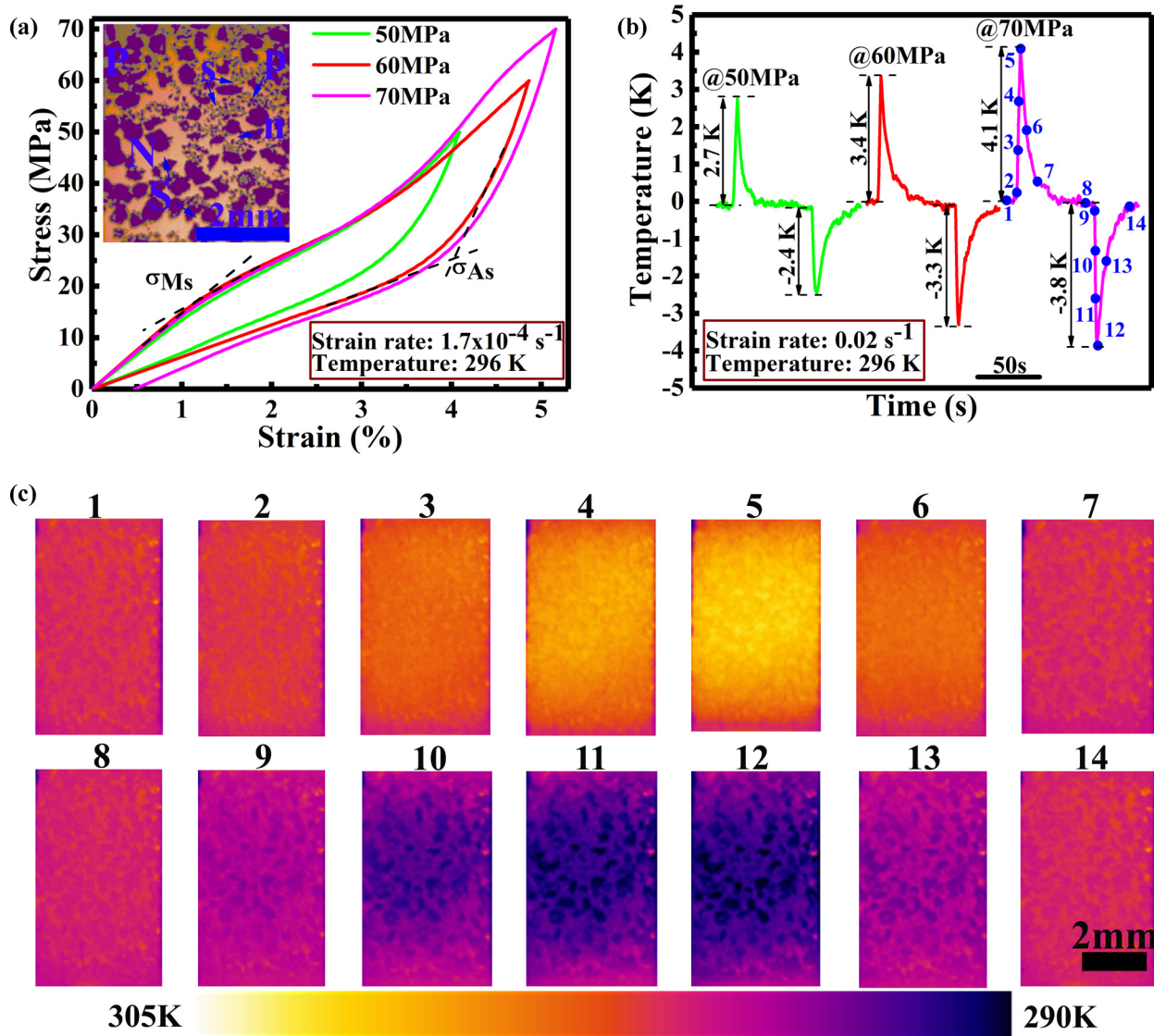
FIG. 2. Superelastic and elastocaloric effects (eCE) in the annealed Ni-Fe-Ga foam. (a) Superelastic stress-strain curves under various stresses 50, 60, and 70 MPa, while the inset shows the architecture of the dual pore foam, (i.e., N: large nodes; P: large pores; S: large struts; n: small nodes; p: small pores and s: small struts), (b) Evolution of the adiabatic temperature change (ΔT_{ad}) during loading and unloading at a strain rate 0.02 s^{-1}, (c) Series of infrared images (time interval between adjacent images is ~0.72 s) showing the temperature evolution during a cycle marked in (b).

to reveal the working stability of the annealed Ni-Fe-Ga foam. It can be seen from Fig. 3(a) that SIMT takes place during the first cycle but shows a residual strain of 0.25% upon unloading. The irreversibility may be ascribed to dislocations produced during SIMT and stabilization of remnant martensite induced by the dislocation strain field [44]. However, the critical stress for the initiation of SIMT gradually decreases during the first 10 cycles (from 11.8 to 10.5 MPa) and then becomes stable due to the training effect [38] as shown in the inset of Fig. 3(a). Interestingly, the critical stress for SIMT rapidly decreases between 175 and 194 cycles [inset of Fig. 3(a)], corresponding to an increase in the maximum strain [Fig. 3(a)], leading to serious damage of the structure after 194 cycles and stop of the test. The corresponding ΔT_{ad} during multiple eCE cycles under an external stress 60 MPa is given in Fig. 3(b). The dual pore foam maintains the good

cyclic stability up to 194 cycles and ΔT_{ad} varies between 2.8–3.1 K and 2.2–3.0 K during loading and unloading, respectively.

The polycrystalline bulk samples deform at various points because the stress-induced martensitic variants emerged asynchronously in different directions under variable strengths, which produce strain incompatibilities resulting in the crack initiation and fracture at grain boundaries [45]. Here, the dual size pores effectively reduce the grain boundary constraints through screening the stresses of strain mismatch, even if the grains span over more than one strut or node [46]. The SIMT is more obvious and homogeneous in thinner struts and nodes in dual pore foam as compared to thick nodes and struts in single pores foam, which implies a higher fraction of materials subjecting to SIMT in dual pore foam. Therefore, the plastic deformation confines at low scale, resulting in
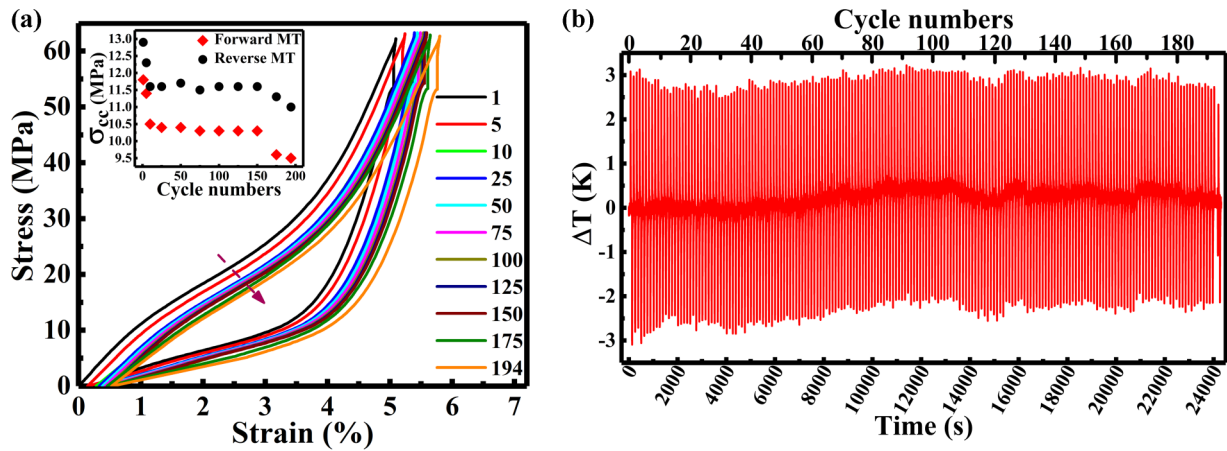
FIG. 3. Superelastic plots and adiabatic temperature change (ΔT_{ad}) during multiple cycles in the annealed Ni-Fe-Ga foam. (a) Compressive cyclic stress-strain curves with the reduction of critical stresses as a function of cycle numbers (in the inset) and corresponding (b) ΔT_{ad} from the test carried out at a temperature 296 K with a strain rate 0.02 s^{-1} under maximum stress 60 MPa.

enhanced ductility in small-sized materials. In addition, the thick nodes store energy during bending/hinging of thin struts (i.e., low energy dissipation during SIMT) that remarkably reduce the hysteresis energy loss during eCE cycling (see Fig. S6 [32]) and thus enhancing the superelastic stability in dual pore foam. Consequently, the hierarchical pore architecture approach in Ni-Fe-Ga alloys produces superior eCE stability over bulk polycrystalline FMSMAs, i.e., single-/dual-phase Ni$_{54}$Fe$_{19}$Ga$_{27}$ [18], Ni$_{45}$Mn$_{36.4}$In$_{13.6}$Co$_5$ [47], and (Ni$_{51.5}$Mn$_{33}$In$_{15.5}$)$_{99.7}$B$_{0.3}$ [38].

To evaluate the cooling efficiency of dual pore foam, the coefficient of performance for material (COP = $\frac{Q}{W}$) [5] can be described by the ratio of cooling power to the mechanical input work. The cooling power ($Q = \Delta T C p \rho$) was estimated from the maximum temperature change of material and the specific heat capacity, while the mechanical input work ($W = \oint \sigma d\varepsilon$) was evaluated by the area enclosed between the loading and unloading stress-strain loop under the assumption of work recovery for all the materials referred in Fig. 4. So, the maximum COP was calculated to be 22 for the current dual pore foam under 70 MPa. As the numbers of stable cycling and materials cooling efficiency are both important, we summarized Ni-Fe-Ga alloys with single-/dual-phase [18] and single [28] /dual pores and some well-studied eCE materials in Fig. 4.

It can be seen from Fig. 4 that the present dual pore foam demonstrates the highest cyclic stability (194 cycles) for polycrystalline Ni-Fe-Ga bulk alloy, i.e., single β phase (10 cycles)/dual-phase (100 cycles) [18] and single pore foam [28] (100 cycles). Moreover, the current cyclic stability (194 cycles) even seems superior to many polycrystalline FMSMAs, e.g., Ni-Mn-In (23 cycles) [38], Ni-Mn-Ga (19 cycles) [54], Ni-Mn-In-Co (15 cycles) [47], Ni-Fe-Mn-Al (30 cycles) [51], (Ni-Mn-In-Cu)B (100 cycles) [23], Ni-Mn-Ga (100 cycles) [22], Co-Ni-Ga single crystals (100 cycles) [36], and some traditional SMAs, i.e., Cu-Zn-Al (100 cycles) [55] and Ni-Ti (100 cycles) [24,56].

Similarly, the dual pore foam exhibits excellent COP (22) over various SMAs (see Fig. 4) and also comparable to single

crystals, i.e., Ni-Fe-Ga (23.3) and Cu-Zn-Al (22.8) [15]; textured polycrystals Ni-Mn-Ga (23.7) [54], conventional polycrystal Ni-Ti-V (22.5) [58], and thin film Ni-Ti-Cu (25.9) [41]. Therefore, the high cyclic stability (194 cycles) and large COP (22) for the dual pore foam indicates that it could be a promising candidate for eCE porous materials.

It is worth noting that very high cyclic stability ($10^4 - 10^6$ cycles) is achieved in single crystals [15] and thin film [19] SMAs but their production is difficult and time consuming [17,21], while NiTi-based alloys degrade remarkably during multiple cycling [41,58]. Conversely, the dual pore foam exhibits stable ΔT_{ad} 2.8 K up to 194 cycles, which demonstrates the possibility of enhancing the working stability via tailoring the materials architecture. Additionally, our work reveals that the porosities of dual pore foam may be feasibly tailored for various applications, e.g., the mechanical properties may be
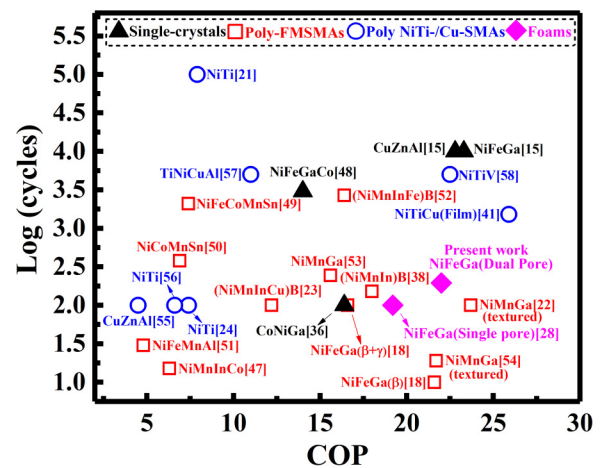

FIG. 4. A comparison of coefficient of performance for materials (COP) and corresponding eCE cycle numbers of the present polycrystalline foam with some well-studied eCE materials, e.g., single crystals [15,36,48], FMSMA polycrystals [18,23,38,47,49–53], textured polycrystals [22,54], conventional polycrystals [21,24,55–58], thin films [41], and single/dual foams [28].

enhanced by designing the pore size equal or smaller than the grain size. Finally, the hierarchical pores foam with large surface areas and porosity can also improve the heat transfer rate and lead to better cooling performance as manifested in active regenerators [59].

However, the fatigue life may be further improved through following possible strategies, for instance, fabricating the mother billets of Ni-Fe-Ga with microalloying the fourth element (Cu, Co, Gd, etc.) [23,49,60], introducing the intergranular secondary (γ-phase) in current B2-structured (β-phase) dual pore foam through annealing [13,18], applying the lower stress to avoid the fracture of thin nodes and struts of dual pore foam and introducing the texture [22,61] in foam through directional solidification after the infiltration process.

What is more, the numerous studies [25,31,62] revealed that FMSMAs foams (i.e., Ni-Mn-Ga) exhibited stable MFIS over millions of cycles ($>10^6$ cycles) under changing magnetic field. As the MFIS was formed in different parts of foam under variable magnetic field, resulting in incompatibility of elongation and shrinkage similar to what happens during applying uniaxial stress, i.e., different stresses exist in nodes and struts of various thickness. This implies that it is possible to achieve a high cyclic stability in foams via appropriate application of the external stress. Consequently, such a well-established strategy is also promising for other polycrystalline FMSMAs with limited eCE stability due to the intrinsic brittleness.

In summary, we demonstrated the enhanced cyclic stability in Ni$_{52.9}$Fe$_{19.2}$Ga$_{27.9}$ foam with 53% porosity and hierarchical pore architecture. The dual pore foam exhibited a high superelastic recovery strain of 4.9% at 296 K under 60 MPa and a large ΔT_{ad} 4.1 K under 70 MPa with high $|\Delta T/\Delta\sigma|$ 58.6 K/GPa through greater SIMT. The greater percentage of SIMT existing in the dual pore foam was related to homogeneous SIMT at thin nodes and struts, and the low hysteresis loss as thick nodes may effectively store the elastic energy produced by thin nodes/struts. Finally, a stable cyclic performance up to 194 cycles with $\Delta T_{ad} \sim 2.8$ K was obtained in the dual pore foam, which was attributed to low hysteresis loss under small stress and high crack initiation/propagation resistance due to dual pore architecture. Although the obtained cyclic stability is much lower than the practical utilization (10^7 cycles) of eCE cooling, it provides a strategy of tuning the materials architecture via a hierarchy of pore sizes in improving the mechanical stability of FMSMAs.

[1] W. Goetzler, R. Zogg, J. Young, and C. Johnson, Energy Savings Potential and RD&D Opportunities for Non-Vapor-Compression HVAC Technologies, U.S. Department of Energy, Report No. DOE/EE-1021 (2014).

[2] E. Bonnot, R. Romero, L. Mañosa, E. Vives, and A. Planes, Phys. Rev. Lett. **100**, 125901 (2008).

[3] L. Mañosa and A. Planes, Adv. Mater. **29**, 1603607 (2017).

[4] J. Tušek, K. Engelbrecht, L.P. Mikkelsen, and N. Pryds, J. Appl. Phys. **117**, 124901 (2015).

[5] J. Cui, Y. M. Wu, J. Muehlbauer, Y. H. Hwang, R. Radermacher, S. Fackler, M. Wuttig, and I. Takeuchi, Appl. Phys. Lett. **101**, 073904 (2012).

[6] S. Xu, H. Y. Huang, J. X. Xie, S. Takekawa, X. Xu, T. Omori, and R. Kainuma, Appl. Mater **4**, 106106 (2016).

[7] J. Wang, Q. Yu, K. Xu, C. Zhang, Y. Wu, and C. Jiang, Scr. Mater. **130**, 148 (2017).

[8] D. W. Zhao, J. Liu, Y. Feng, W. Sun, and A. Yan, Appl. Phys. Lett. **110**, 021906 (2017).

[9] Y. Li, D. Zhao, J. Liu, S. Qian, Z. Li, W. Gan, and X. Chen, ACS Appl. Mater. Inter. **10**, 25438 (2018).

[10] S. X. Qian, Y. L. Geng, Y. Wang, J. Z. Ling, Y. H. Hwang, R. Radermacher, I. Takeuchi, and J. Cui, Int. J. Refrig. **64**, 1 (2016).

[11] W. Sun, J. Liu, B. F. Lu, Y. Li, and A. Yan, Scr. Mater. **114**, 1 (2016).

[12] Y. Li, D. Zhao, and J. Liu, Sci Rep-Uk **6**, 25500 (2016).

[13] K. Oikawa, T. Ota, T. Ohmori, Y. Tanaka, H. Morito, A. Fujita, R. Kainuma, K. Fukamichi, and K. Ishida, Appl. Phys. Lett. **81**, 5201 (2002).

[14] C. Efstathiou, H. Sehitoglu, P. Kurath, S. Foletti, and P. Davoli, Scr. Mater. **57**, 409 (2007).

[15] Y. Wu, E. Ertekin, and H. Sehitoglu, Acta Mater. **135**, 158 (2017).

[16] G. J. Pataky, E. Ertekin, and H. Sehitoglu, Acta Mater. **96**, 420 (2015).

[17] K. Ullakko, Y. Ezer, A. Sozinov, G. Kimmel, P. Yakovenko, and V. K. Lindroos, Scr. Mater. **44**, 475 (2001).

[18] Y. Xu, B. Lu, W. Sun, A. Yan, and J. Liu, Appl. Phys. Lett. **106**, 201903 (2015).

[19] C. Chluba, W. W. Ge, R. L. de Miranda, J. Strobel, L. Kienle, E. Quandt, and M. Wuttig, Science **348**, 1004 (2015).

[20] H. Hou, J. Cui, S. Qian, D. Catalini, Y. Hwang, R. Radermacher, and I. Takeuchi, MRS Bull. **43**, 285 (2018).

[21] J. Tušek, A. Žerovnik, M. Čebron, M. Brojan, B. Žužek, K. Engelbrecht, and A. Cadelli, Acta Mater. **150**, 295 (2018).

[22] L. Wei, X.X. Zhang, J. Liu, and L. Geng, AIP Adv. **8**, 055312 (2018).

[23] X. Tang, Y. Feng, H. Wang, and P. Wang, Appl. Phys. Lett. **114**, 033901 (2019).

[24] H. Chen, F. Xiao, X. Liang, Z. Li, Z. Li, X. Jin, N. Min, and T. Fukuda, Scr. Mater. **162**, 230 (2019).

[25] Y. Boonyongmaneerat, M. Chmielus, D. C. Dunand, and P. Müllner, Phys. Rev. Lett. **99**, 247201 (2007).

[26] J. Lyubina, R. Schafer, N. Martin, L. Schultz, and O. Gutfleisch, Adv. Mater. **22**, 3735 (2010).

[27] M. Imran and X. Zhang, J. Phys. D **53**, 245503 (2020).

[28] M. Imran, X. Zhang, M. Qian, and L. Geng, Adv. Eng. Mater. **22**, 1901140 (2020).

[29] C.P. Sasso, P. Zheng, V. Basso, P. Müllner, and D.C. Dunand, Intermetallics **19**, 952 (2011).

[30] J. Tušek, K. Engelbrecht, D. Eriksen, S. Dall'Olio, J. Tušek, and N. Pryds, Nat. Energy **1**, 16134 (2016).

[31] X. X. Zhang, C. Witherspoon, P. Müllner, and D. C. Dunand, Acta Mater. **59**, 2229 (2011).

[32] See Supplemental Material at http://link.aps.org/supplemental/10.1103/PhysRevMaterials.4.065403 for materials preparation, characterization, and temperature-dependent superelastic phenomenon along with the transition entropy change and the hysteresis energy loss under eCE cycling.

[33] L. J. Gibson and M. F. Ashby, *Cellular Solids: Structure and Properties*, 2nd ed. (Cambridge University Press, Cambridge, 1997).

[34] T. Aydogmus and S. Bor, J. Alloy. Compd. **478**, 705 (2009).

[35] B. Yuan, P. Zheng, Y. Gao, M. Zhu, and D. C. Dunand, Mater. Des. **80**, 28 (2015).

[36] A. Shen, D. W. Zhao, W. Sun, J. Liu, and C. J. Li, Scr. Mater. **127**, 1 (2017).

[37] F. Xiao, T. Fukuda, T. Kakeshita, and X. J. Jin, Acta Mater. **87**, 8 (2015).

[38] Z. Yang, D. Y. Cong, X. M. Sun, Z. H. Nie, and Y. D. Wang, Acta Mater. **127**, 33 (2017).

[39] B. F. Lu, F. Xiao, A. Yan, and J. Liu, Appl. Phys. Lett. **105**, 161905 (2014).

[40] S. Qian, Y. L. Geng, Y. Wang, T. E. Pillsbury, Y. Hada, Y. Yamaguchi, K. Fujimoto, Y. H. Hwang, R. Radermacher, J. Cui, Y. J. Yuki, K. Toyotake, and I. Takeuchi, Philos. T. R. Soc. A **374**, 20150309 (2016).

[41] C. Bechtold, C. Chluba, R. L. De Miranda, and E. Quandt, Appl. Phys. Lett. **101**, 091903 (2012).

[42] M. Panico and L. C. Brinson, Int. J. Solids Struct. **45**, 5613 (2008).

[43] H. Li, B. Yuan, and Y. Gao, J. Alloys Compd. **767**, 690 (2018).

[44] D. Cong, G. Saha, and M. Barnett, Acta Biomater. **10**, 5178 (2014).

[45] S.M. Ueland and C.A. Schuh, J. Appl. Phys. **114**, 053503 (2013).

[46] M. Chmielus, C. Witherspoon, R. C. Wimpory, A. Paulke, A. Hilger, X. X. Zhang, D. C. Dunand, and P. Müllner, J. Appl. Phys. **108**, 123526 (2010).

[47] B. F. Lu, P. N. Zhang, Y. Xu, W. Sun, and J. Liu, Mater. Lett. **148**, 110 (2015).

[48] F. Xiao, M. J. Jin, J. Liu, and X. J. Jin, Acta Mater. **96**, 292 (2015).

[49] Y. Qu, A. Gràcia-Condal, L. Mañosa, A. Planes, D. Cong, Z. Nie, Y. Ren, and Y. Wang, Acta Mater. **177**, 46 (2019).

[50] Y. H. Qu, D. Y. Cong, S. H. Li, W. Y. Gui, Z. H. Nie, M. H. Zhang, Y. Ren, and Y. D. Wang, Acta Mater. **151**, 41 (2018).

[51] T. Cao, H. Xuan, S. Liu, L. Wang, Z. Xie, X. Liang, F. Chen, P. Han, D. Wang, and Y. Du, Intermetallics **112**, 106529 (2019).

[52] Z. Yang, D. Y. Cong, Y. Yuan, Y. Wu, Z. H. Nie, R. G. Li, and Y. D. Wang, Mater. Res. Lett. **7**, 137 (2019).

[53] L. Wei, X. X. Zhang, W. Gan, C. Ding, and L. Geng, Scr. Mater. **168**, 28 (2019).

[54] D. Li, Z. Li, J. Yang, Z. Li, B. Yang, H. Yan, D. Wang, L. Hou, X. Li, Y. Zhang, C. Esling, X. Zhao, and L. Zuo, Scr. Mater. **163**, 116 (2019).

[55] L. Mañosa, S. Jarque-Farnos, E. Vives, and A. Planes, Appl. Phys. Lett. **103**, 211904 (2013).

[56] M. Zhou, Y. Li, C. Zhang, S. Li, E. Wu, W. Li, and L. Li, J. Phys. D **51**, 135303 (2018).

[57] H. Chen, F. Xiao, X. Liang, Z. Li, X. Jin, and T. Fukuda, Acta Mater. **158**, 330 (2018).

[58] Y. Kim, M.-G. Jo, J.-W. Park, H.-K. Park, and H. N. Han, Scr. Mater. **144**, 48 (2018).

[59] J. Tušek, K. Engelbrecht, R. Millan-Solsona, L. Manosa, E. Vives, L. P. Mikkelsen, and N. Pryds, Adv. Energy Mater. **5**, 1500361 (2015).

[60] H. Xuan, T. Cao, S. Li, L. Wang, Z. Xie, X. Liang, F. Chen, and P. Han, Solid State Commun. **301**, 113706 (2019).

[61] W. Sun, J. Liu, D. Zhao, and M. Zhang, J. Phys. D **50**, 444001 (2017).

[62] M. Chmielus, X. X. Zhang, C. Witherspoon, D. C. Dunand, and P. Müllner, Nat. Mater. **8**, 863 (2009).